A flat Universe from high-resolution maps of the cosmic microwave background radiation

P. de Bernardis[1], P. A. R. Ade[2], J. J. Bock[3], J. R. Bond[4], J. Borrill[5,12], A. Boscaleri[6], K. Coble[7], B. P. Crill[8], G. De Gasperis[9], P. C. Farese[7], P. G. Ferreira[10], K. Ganga[8,11], M. Giacometti[1], E. Hivon[8], V. V. Hristov[8], A. Iacoangeli[1], A. H. Jaffe[12], A. E. Lange[8], L. Martinis[13], S. Masi[1], P. V. Mason[8], P. D. Mauskopf[14,15], A. Melchiorri[1], L. Miglio[16], T. Montroy[7], C. B. Netterfield[16], E. Pascale[6], F. Piacentini[1], D. Pogosyan[4], S. Prunet[4], S. Rao[17], G. Romeo[17], J. E. Ruhl[7], F. Scaramuzzi[13], D. Sforna[1] & N. Vittorio[9]

The blackbody radiation left over from the Big Bang has been transformed by the expansion of the Universe into the nearly isotropic 2.73 K cosmic microwave background. Tiny inhomogeneities in the early Universe left their imprint on the microwave background in the form of small anisotropies in its temperature. These anisotropies contain information about basic cosmological parameters, particularly the total energy density and curvature of the Universe. Here we report the first images of resolved structure in the microwave background anisotropies over a significant part of the sky. Maps at four frequencies clearly distinguish the microwave background from foreground emission. We compute the angular power spectrum of the microwave background, and find a peak at Legendre multipole $l_{peak} = (197 \pm 6)$, with an amplitude $\Delta T_{200} = (69 \pm 8)\ \mu K$. This is consistent with that expected for cold dark matter models in a flat (euclidean) Universe, as favoured by standard inflationary models.

Photons in the early Universe were tightly coupled to ionized matter through Thomson scattering. This coupling ceased about 300,000 years after the Big Bang, when the Universe cooled sufficiently to form neutral hydrogen. Since then, the primordial photons have travelled freely through the Universe, redshifting to microwave frequencies as the Universe expanded. We observe those photons today as the cosmic microwave background (CMB). An image of the early Universe remains imprinted in the temperature anisotropy of the CMB. Anisotropies on angular scales larger than $\sim 2^\circ$ are dominated by the gravitational redshift the photons undergo as they leave the density fluctuations present at decoupling[1,2]. Anisotropies on smaller angular scales are enhanced by oscillations of the photon–baryon fluid before decoupling[3]. These oscillations are driven by the primordial density fluctuations, and their nature depends on the matter content of the Universe.

In a spherical harmonic expansion of the CMB temperature field, the angular power spectrum specifies the contributions to the fluctuations on the sky coming from different multipoles l, each corresponding to the angular scale $\theta = \pi/l$. Density fluctuations over spatial scales comparable to the acoustic horizon at decoupling produce a peak in the angular power spectrum of the CMB, occurring at multipole l_{peak}. The exact value of l_{peak} depends on both the linear size of the acoustic horizon and on the angular diameter distance from the observer to decoupling. Both these quantities are sensitive to a number of cosmological parameters (see, for example, ref. 4), but l_{peak} primarily depends on the total density of the Universe, Ω_0. In models with a density Ω_0 near 1, $l_{peak} \approx 200/\Omega_0^{1/2}$. A precise measurement of l_{peak} can efficiently constrain the density and thus the curvature of the Universe.

Observations of CMB anisotropies require extremely sensitive and stable instruments. The DMR[5] instrument on the COBE satellite mapped the sky with an angular resolution of $\sim 7^\circ$, yielding measurements of the angular power spectrum at multipoles $l < 20$. Since then, experiments with finer angular resolution[6–16] have detected CMB fluctuations on smaller scales and have produced evidence for the presence of a peak in the angular power spectrum at $l_{peak} \approx 200$.

Here we present high-resolution, high signal-to-noise maps of the CMB over a significant fraction of the sky, and derive the angular power spectrum of the CMB from $l = 50$ to 600. This power spectrum is dominated by a peak at multipole $l_{peak} = (197 \pm 6)$ (1σ error). The existence of this peak strongly supports inflationary models for the early Universe, and is consistent with a flat, euclidean Universe.

The instrument

The Boomerang (balloon observations of millimetric extragalactic radiation and geomagnetics) experiment is a microwave telescope that is carried to an altitude of ~ 38 km by a balloon. Boomerang combines the high sensitivity and broad frequency coverage pioneered by an earlier generation of balloon-borne experiments with the long (~ 10 days) integration time available in a long-duration balloon flight over Antarctica. The data described here were obtained with a focal plane array of 16 bolometric detectors cooled to 0.3 K. Single-mode feedhorns provide two 18′ full-width at half-maximum (FWHM) beams at 90 GHz and two 10′ FWHM beams at 150 GHz. Four multi-band photometers each provide a 10.5′, 14′ and 13′ FWHM beam at 150, 240 and 400 GHz respectively. The average in-flight sensitivity to CMB anisotropies was 140, 170, 210 and 2,700 $\mu K\ s^{1/2}$ at 90, 150, 240 and 400 GHz, respectively. The entire optical system is heavily baffled against terrestrial radiation. Large sunshields improve rejection of radiation from $>60^\circ$ in azimuth from the telescope boresight. The rejection has been measured to be greater than 80 dB at all angles occupied by the Sun during the CMB observations. Further details on the instrument can be found in refs 17–21.

[1] Dipartimento di Fisica, Universita' di Roma "La Sapienza", P.le A. Moro 2, 00185 Roma, Italy. [2] Department of Physics, Queen Mary and Westfield College, Mile End Road, London E1 4NS, UK. [3] Jet Propulsion Laboratory, Pasadena, California 91109, USA. [4] CITA University of Toronto, Toronto M5S 3H8, Canada. [5] NERSC-LBNL, Berkeley, California 94720, USA. [6] IROE–CNR, Via Panciatichi 64, 50127 Firenze, Italy. [7] Department of Physics, University of California at Santa Barbara, Santa Barbara, California 93106, USA. [8] California Institute of Technology, Mail Code 59-33, Pasadena, California 91125, USA. [9] Dipartimento di Fisica, Universita' di Roma Tor Vergata, Via della Ricerca Scientifica 1, 00133 Roma, Italy. [10] Astrophysics, University of Oxford, Keble Road, OX1 3RH, UK. [11] PCC, College de France, 11 pl. Marcelin Berthelot, 75231 Paris Cedex 05, France. [12] Center for Particle Astrophysics, University of California at Berkeley, 301 Le Conte Hall, Berkeley, California 94720, USA. [13] ENEA Centro Ricerche di Frascati, Via E. Fermi 45, 00044 Frascati, Italy. [14] Physics and Astronomy Department, Cardiff University, Cardiff CF2 3YB, UK. [15] Department of Physics and Astronomy, University of Massachusetts, Amherst, Massachusetts 01003, USA. [16] Department of Physics and Astronomy, University of Toronto, Toronto M5S 3H8, Canada. [17] Istituto Nazionale di Geofisica, Via di Vigna Murata 605, 00143, Roma, Italy.

© 2000 Macmillan Magazines Ltd

Observations

Boomerang was launched from McMurdo Station (Antarctica) on 29 December 1998, at 3:30 GMT. Observations began 3 hours later, and continued uninterrupted during the 259-hour flight. The payload approximately followed the 79° S parallel at an altitude that varied daily between 37 and 38.5 km, returning within 50 km of the launch site.

We concentrated our observations on a target region, centred at roughly right ascension (RA) 5h, declination (dec.) –45°, that is uniquely free of contamination by thermal emission from interstellar dust[22] and that is approximately opposite the Sun during the austral summer. We mapped this region by repeatedly scanning the telescope through 60° at fixed elevation and at constant speed. Two scan speeds (1° s^{-1} and 2° s^{-1} in azimuth) were used to facilitate tests for systematic effects. As the telescope scanned, degree-scale variations in the CMB generated sub-audio frequency signals in the output of the detector[23]. The stability of the detector system was sufficient to allow sensitive measurements on angular scales up to tens of degrees on the sky. The scan speed was sufficiently rapid with respect to sky rotation that identical structures were observed by

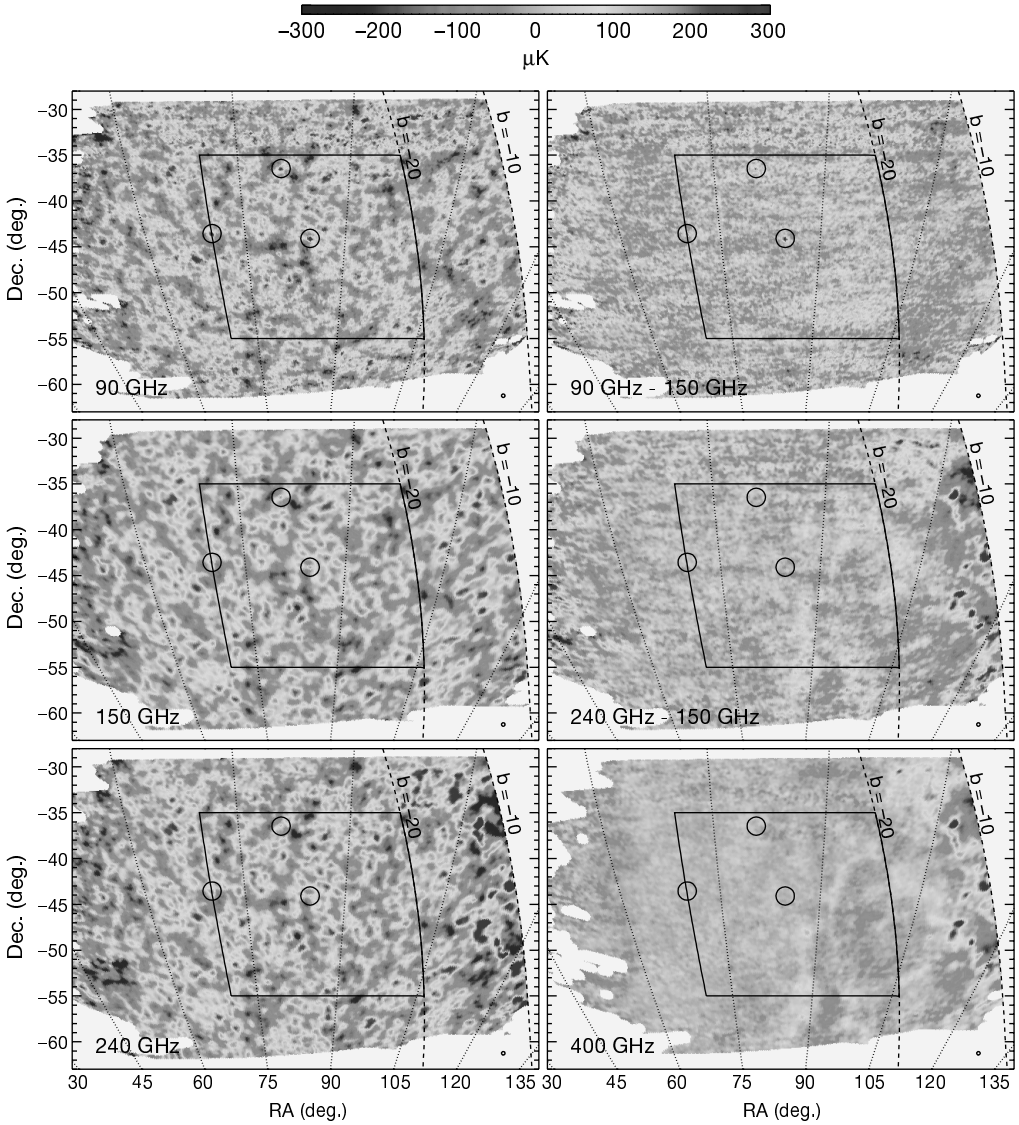

Figure 1 Boomerang sky maps (equatorial coordinates). The sky maps at 90, 150 and 240 GHz (left panels) are shown with a common colour scale, using a thermodynamic temperature scale chosen such that CMB anisotropies will have the same amplitude in the three maps. Only the colour scale of the 400 GHz map (bottom right) is 14 times larger than the others: this has been done to facilitate comparison of emission from interstellar dust (ISD), which dominates this map, with ISD emission present in the lower-frequency maps. The maps at 90 and 400 GHz are each from a single detector, while maps at 150 and 240 GHz have each been obtained by co-adding data from three detectors. For purposes of presentation, the maps have been smoothed with gaussian filters to obtain FWHM effective resolution of 22.5′ (small circle in the bottom right side of each panel). Structures along the scan direction larger than 10° are not present in the maps. Several features are immediately evident. Most strikingly, the maps at 90, 150 and 240 GHz are dominated by degree-scale structures that fill the map, have well-correlated morphology and are identical in amplitude in all three maps. These structures are not visible at 400 GHz. The 400 GHz map is dominated by diffuse emission which is correlated with the ISD emission mapped by IRAS/DIRBE[22]. This emission is strongly concentrated towards the right-hand edge of the maps, near the plane of the Galaxy. The same structures are evident in the 90, 150 and 240 GHz maps at Galactic latitude $b > -15°$, albeit with an amplitude that decreases steeply with decreasing frequency. The large-scale gradient evident especially near the right edge of the 240 GHz map is a result of high-pass-filtering the very large signals near the Galactic plane (not shown). This effect is negligible in the rest of the map. The two top right panels show maps constructed by differencing the 150 and 90 GHz maps and the 240 and 150 GHz maps. The difference maps contain none of the structures that dominate the maps at 90, 150 and 240 GHz, indicating that these structures do indeed have the ratios of brightness that are unique to the CMB. The morphology of the residual structures in the 240–150 GHz map is well-correlated with the 400 GHz map, as is expected if the residuals are due to the ISD emission. Three compact sources of emission are visible in the lower-frequency maps, as indicated by the circles. These are known radio-bright quasars from the SEST pointing catalogue at 230 GHz. The boxed area has been used for computing the angular power spectrum shown in Fig. 2.

© 2000 Macmillan Magazines Ltd

detectors in the same row in each scan. Detectors in different rows observed the same structures delayed in time by a few minutes.

At intervals of several hours, the telescope elevation was interchanged between 40°, 45° and 50° in order to increase the sky coverage and to provide further systematic tests. Sky rotation caused the scan centre to move and the scan direction to rotate on the celestial sphere. A map from a single day at a single elevation covered roughly 22° in declination and contained scans rotated by ±11° on the sky, providing a cross-linked scan pattern. Over most of the region mapped, each sky pixel was observed many times on different days, both at $1^\circ\,s^{-1}$ and $2^\circ\,s^{-1}$ scan speed, with different topography, solar elongation and atmospheric conditions, allowing strong tests for any contaminating signal not fixed on the celestial sphere.

The pointing of the telescope has been reconstructed with an accuracy of 2′ r.m.s. using data from a Sun sensor and rate gyros. This precision has been confirmed by analysing the observed positions of bright compact H II regions in the Galactic plane (RCW38[24], RCW57, IRAS08576 and IRAS1022) and of radio-bright point sources visible in the target region (the QSO 0483–436, the BL Lac object 0521–365 and the blazar 0537–441).

Calibrations

The beam pattern for each detector was mapped before flight using a thermal source. The main lobe at 90, 150 and 400 GHz is accurately modelled by a gaussian function. The 240 GHz beams are well modelled by a combination of two gaussians. The beams have small shoulders (less than 1% of the total solid angle), due to aberrations in the optical system. The beam-widths were confirmed in flight via observations of compact sources. By fitting radial profiles to these sources we determine the effective angular resolution, which includes the physical beamwidth and the effects of the 2′ r.m.s. pointing jitter. The effective FWHM angular resolution of the 150 GHz data that we use here to calculate the CMB power spectrum is (10 ± 1)′, where the error is dominated by uncertainty in the pointing jitter.

We calibrated the 90, 150 and 240 GHz channels from their measured response to the CMB dipole. The dipole anisotropy has been accurately (0.7%) measured by COBE-DMR[25], fills the beam and has the same spectrum as the CMB anisotropies at smaller angular scales, making it the ideal calibrator for CMB experiments. The dipole signal is typically ~3 mK peak-to-peak in each 60° scan, much larger than the detector noise, and appears in the output of the detectors at $f = 0.008$ Hz and $f = 0.016$ Hz in the $1^\circ\,s^{-1}$ and $2^\circ\,s^{-1}$ scan speeds, respectively. The accuracy of the calibration is dominated by two systematic effects: uncertainties in the low-frequency transfer function of the electronics, and low-frequency, scan-synchronous signals. Each of these is significantly different at the two scan speeds. We found that the dipole-fitted amplitudes derived from separate analysis of the $1^\circ\,s^{-1}$ and $2^\circ\,s^{-1}$ data agree to within ±10% for every channel, and thus we assign a 10% uncertainty in the absolute calibration.

Table 1 Angular power spectrum of CMB anisotropy

l range	150 GHz ([1st half] + [2nd half])/2	150 GHz ([1st half] − [2nd half])/2
26–75	1,140 ± 280	63 ± 32
76–125	3,110 ± 490	16 ± 20
126–175	4,160 ± 540	17 ± 28
176–225	4,700 ± 540	59 ± 44
226–275	4,300 ± 460	68 ± 59
276–325	2,640 ± 310	130 ± 82
326–375	1,550 ± 220	−7 ± 92
376–425	1,310 ± 220	−60 ± 120
426–475	1,360 ± 250	0 ± 160
476–525	1,440 ± 290	220 ± 230
526–575	1,750 ± 370	130 ± 300
576–625	1,540 ± 430	−430 ± 360

Shown are measurements of the angular power spectrum of the cosmic microwave background at 150 GHz, and tests for systematic effects. The values listed are for $\Delta T_l^2 = l(l+1)c_l/2\pi$, in μK^2. Here $c_l = \langle a_{lm}^2 \rangle$, and a_{lm} are the coefficients of the spherical harmonic decomposition of the CMB temperature field: $\Delta T(\theta,\phi) = \Sigma a_{lm} Y_{lm}(\theta,\phi)$. The stated 1σ errors include statistical and cosmic/sample variance, and do not include a 10% calibration uncertainty.

From detector signals to CMB maps

The time-ordered data comprises 5.4×10^7 16-bit samples for each channel. These data are flagged for cosmic-ray events, elevation changes, focal-plane temperature instabilities, and electromagnetic interference events. In general, about 5% of the data for each channel are flagged and not used in the subsequent analysis. The gaps resulting from this editing are filled with a constrained realization of noise in order to minimize their effect in the subsequent filtering of the data. The data are deconvolved by the bolometer and electronics transfer functions to recover uniform gain at all frequencies.

The noise power spectrum of the data and the maximum-likelihood maps[26–28] were calculated using an iterative technique[29] that separates the sky signal from the noise in the time-ordered data. In this process, the statistical weights of frequencies corresponding to angular scales larger than 10° on the sky are set to zero to filter out the largest-scale modes of the map. The maps were pixelized according to the HEALPix pixelization scheme[30].

Figure 1 shows the maps obtained in this way at each of the four frequencies. The 400 GHz map is dominated by emission from interstellar dust that is well correlated with that observed by the IRAS and COBE/DIRBE satellites. The 90, 150 and 240 GHz maps are dominated by degree-scale structures that are resolved with high signal-to-noise ratio. A qualitative but powerful test of the hypothesis that these structures are CMB anisotropy is provided by subtracting one map from another. The structures evident in all

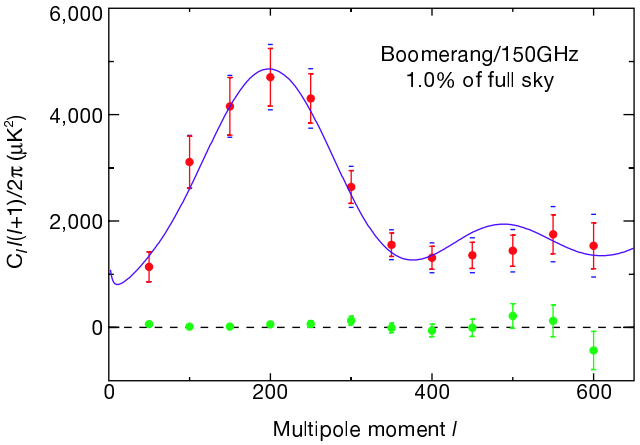

Figure 2 Angular power spectrum measured by Boomerang at 150 GHz. Each point is the power averaged over $\Delta l = 50$ and has negligible correlations with the adjacent points. The error bars indicate the uncertainty due to noise and cosmic/sampling variance. The errors are dominated by cosmic/sampling variance at $l < 350$; they grow at large l due to the signal attenuation caused by the combined effects[39] of the 10′ beam and the 14′ pixelization (0.87 at $l = 200$ and 0.33 at $l = 600$). The current ±10% uncertainty in the calibration corresponds to an overall re-scaling of the y-axis by ±20%, and is not shown. The current 1′ uncertainty in the angular resolution of the measurement creates an additional uncertainty—indicated by the distance between the ends of the red error bars and the blue horizontal lines—that is completely correlated and is largest (11%) at $l = 600$. The green points show the power spectrum of a difference map obtained as follows. We divided the data into two parts corresponding to the first and second halves of the timestream. We made two maps (A and B) from these halves, and the green points show the power spectrum computed from the difference map, (A–B)/2. Signals originating from the sky should disappear in this map, so this is a test for contamination in the data (see text). The solid curve has parameters $(\Omega_b, \Omega_m, \Omega_\Lambda, n_s, h) = (0.05, 0.31, 0.75, 0.95, 0.70)$. It is the best-fit model for the Boomerang test flight data[15,16], and is shown for comparison only. The model that best fits the new data reported here will be presented elsewhere.

© 2000 Macmillan Magazines Ltd

three maps disappear in both the 90–150 GHz difference and in the 240–150 GHz difference, as expected for emission that has the same spectrum as the CMB dipole anisotropy used to calibrate the maps.

To quantify this conclusion, we performed a 'colour index' analysis of our data. We selected the ~18,000 14′ pixels at Galactic latitude $b < -15°$, and made scatter plots of 90 GHz versus 150 GHz and 240 GHz versus 150 GHz. A linear fit to these scatter plots gives slopes of 1.00 ± 0.15 and 1.10 ± 0.16, respectively (including our present 10% calibration error), consistent with a CMB spectrum. For comparison, free–free emission with spectral index −2.35 would produce slopes of 2.3 and 0.85, and was therefore rejected with >99% confidence; emission from interstellar dust with temperature $T_d = 15$ K and spectral index of emissivity $\alpha = 1$ would produce slopes of 0.40 and 2.9. For any combination of $T_d > 7$ K and $1 < \alpha < 2$, the dust hypothesis is rejected with >99% confidence. We conclude that the dominant source of structure that we detect at 90, 150 and 240 GHz is CMB anisotropy.

We further argue that the 150 GHz map at $b < -15°$ is free of significant contamination by any known astrophysical foreground. Galactic synchrotron and free–free emission is negligible at this frequency[31]. Contamination from extragalactic point sources is also small[32]; extrapolation of fluxes from the PMN survey[33] limits the contribution by point sources (including the three above-mentioned radio-bright sources) to the angular power spectrum derived below to <0.7% at $l = 200$ and <20% at $l = 600$. The astrophysical foreground that is expected to dominate at 150 GHz is thermal emission from interstellar dust. We placed a quantitative limit on this source of contamination as follows. We assumed that dust properties are similar at high ($b < -20°$) and moderate ($-20° < b < -5°$) Galactic latitudes. We selected the pixels at moderate Galactic latitudes and correlated the structure observed in each of our four bands with the IRAS/DIRBE map, which is dominated by dust in cirrus clouds. The best-fit slope of each of the scatter plots measures the ratios of the dust signal in the Boomerang channels to the dust signal in the IRAS/DIRBE map. We found that the 400 GHz map is very well correlated to the IRAS/DIRBE map, and that dust at $b < -20°$ can account for at most 10% of the signal variance at 240 GHz, 3% at 150 GHz and 0.5% at 90 GHz.

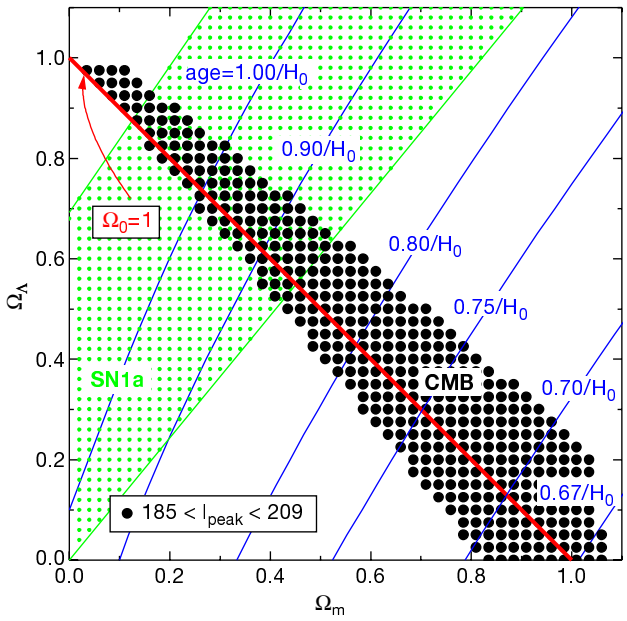

Figure 3 Observational constraints on Ω_m and Ω_Λ. All the cosmological models (from our data base) consistent with the position of the peak in the angular power spectrum measured by Boomerang (95% confidence intervals) define an "allowed" region in the $\Omega_m - \Omega_\Lambda$ plane (marked by large black dots). Such a region is elongated around the $\Omega_0 = 1$ line identifying a flat geometry, euclidean Universe. The blue lines define the age of the Universe for the considered models. The green-dotted region is consistent (95% confidence contour) with the recent results of the high-redshift supernovae surveys[40,41].

Angular power spectra

We compared the angular power spectrum of the structures evident in Fig. 1 with theoretical predictions. In doing so, we separated and removed the power due to statistical noise and systematic artefacts from the power due to the CMB anisotropies in the maps. The maximum-likelihood angular power spectrum of the maps was computed using the MADCAP[34] software package, whose algorithms fully take into account receiver noise and filtering.

Full analysis of our entire data set is under way. Because of the computational intensity of this process, we report here the results of a complete analysis of a limited portion of the data chosen as follows. We analysed the most sensitive of the 150 GHz detectors. We restricted the sky coverage to an area with RA > 70°, $b < -20°$ and $-55° <$ dec. $< -35°$, and we used only the ~50% of the data from this detector that was obtained at a scan speed of $1° s^{-1}$. We used a relatively coarse pixelization of 8,000 14-arcmin pixels as a compromise between computation speed and coverage of high multipoles. Finally, we limited our analysis to $l \leqslant 600$ for which the effects of pixel shape and size and our present uncertainty in the beam size (1′) are small and can be accurately modelled.

The angular power spectrum determined in this way is shown in Fig. 2 and reported in Table 1. The power spectrum is dominated by a peak at $l_{peak} \approx 200$, as predicted by inflationary cold dark matter models. These models additionally predict the presence of secondary peaks. The data at high l limit the amplitude, but do not exclude the presence, of a secondary peak. The errors in the angular power spectrum are dominated at low multipoles ($l \lesssim 350$) by the cosmic/sampling variance, and at higher multipoles by detector noise.

The CMB angular power spectrum shown in Fig. 2 was derived from 4.1 days of observation. As a test of the stability of the result, we made independent maps from the first and second halves of these data. The payload travels several hundred kilometres, and the Sun moves 2° on the sky, between these maps. Comparing them provides a stringent test for contamination from sidelobe pickup and thermal effects. The angular power spectrum calculated for the difference map is shown in Fig. 2. The reduced χ^2 of this power spectrum with respect to zero signal is 1.11 (12 degrees of freedom), indicating that the difference map is consistent with zero contamination.

A peak at $l \approx 200$ implies a flat Universe

The location of the first peak in the angular power spectrum of the CMB is well measured by the Boomerang data set. From a parabolic fit to the data at $l = 50$ to 300 in the angular power spectrum, we find $l_{peak} = (197 \pm 6)$ (1σ error). The parabolic fit does not bias the determination of the peak multipole: applying this method to Monte Carlo realizations of theoretical power spectra we recover the correct peak location for a variety of cosmological models. Finally, the peak location is independent of the details of the data calibration, which obviously affect only the height of the peak and not its location. The height of the peak is $\Delta T_{200} = (69 \pm 4) \pm 7$ μK (1σ statistical and calibration errors, respectively).

The data are inconsistent with current models based on topological defects (see, for example, ref. 35) but are consistent with a subset of cold dark matter models. We generated a database of cold dark matter models[36,37], varying six cosmological parameters (the range of variation is given in parentheses): the non-relativistic matter density, Ω_m (0.05–2); the cosmological constant, Ω_Λ (0–1); the Hubble constant, h (0.5–0.8); the baryon density, $h^2\Omega_b$ (0.013–0.025), the primordial scalar spectral index, n_s (0.8–1.3); and the overall normalization A (free parameter) of the primordial density fluctuation power spectrum. We compared these models with the power spectrum we report here to place constraints on

© 2000 Macmillan Magazines Ltd

allowed regions in this 6-parameter space. In Figure 3 we mark with large black dots the region of the Ω_m–Ω_Λ plane where some combination of the remaining four parameters within the ranges defined by our model space gives a power spectrum consistent with our 95% confidence interval for l_{peak}. This region is quite narrow, and elongated along the 'flat Universe' line $\Omega_m + \Omega_\Lambda = 1$. The width of this region is determined by degeneracy in the models, which produce closely similar spectra for different values of the parameters[38]. We further evaluated the likelihood of the models given the Boomerang measurement and the same priors (constraints on the values of the cosmological parameters) as in ref. 16. Marginalizing over all the other parameters, we found the following 95% confidence interval for $\Omega_0 = \Omega_m + \Omega_\Lambda$: $0.88 < \Omega_0 < 1.12$. This provides evidence for a euclidean geometry of the Universe. Our data clearly show the presence of power beyond the peak at $l = 197$, corresponding to smaller-scale structures. The consequences of this fact will be fully analysed elsewhere. □

Received 24 March; accepted 3 April 2000.

1. Sachs, R. K. & Wolfe, A. M. Perturbations of a cosmological model and angular variations of the microwave background. *Astrophys. J.* **147**, 73–90 (1967).
2. Weinberg S., *Gravitation and Cosmology* (Wiley & Sons, New York, 1972).
3. Hu, W., Sugiyama, N. & Silk, J. The physics of cosmic microwave background anisotropies. *Nature* **386,** 37–43 (1997).
4. Bond, J. R., Efstathiou, G. & Tegmark, M. Forecasting cosmic parameter errors from microwave background anisotropy experiments. *Mon Not. R. Astron. Soc.* **291,** L33–L41 (1997).
5. Hinshaw, G. *et al.* Band power spectra in the COBE-DMR four-year anisotropy map. *Astrophys. J.* **464,** L17–L20 (1996).
6. Scott, P. F. *et al.* Measurement of structure in the cosmic background radiation with the Cambridge cosmic anisotropy telescope. *Astrophys. J.* **461,** L1–L4 (1996).
7. Netterfield, C. B. *et al.* A measurement of the angular power spectrum of the anisotropy in the cosmic microwave background. *Astrophys. J.* **474,** 47–66 (1997).
8. Leitch, E. M. *et al.* A measurement of anisotropy in the cosmic microwave background on 7-22 arcminute scales. *Astrophys. J.* (submitted); also as preprint astro-ph/9807312 at ⟨http://xxx.lanl.gov⟩ (1998).
9. Wilson, G. W. *et al.* New CMB power spectrum constraints from MSAMI. *Astrophys. J.* (submitted); also as preprint astro-ph/9902047 at ⟨http://xxx.lanl.gov⟩ (1999).
10. Baker, J. C. *et al.* Detection of cosmic microwave background structure in a second field with the cosmic anisotropy telescope. *Mon Not. R. Astron. Soc.* (submitted); also as preprint astro-ph/9904415 at ⟨http://xxx.lanl.gov⟩ (1999).
11. Peterson, J. B. *et al.* First results from Viper: detection of small-scale anisotropy at 40 GHZ. Preprint astro-ph/9910503 at ⟨http://xxx.lanl.gov⟩ (1999).
12. Coble, K. *et al.* Anisotropy in the cosmic microwave background at degree angular scales: Python V results. *Astrophys. J.* **519,** L5–L8 (1999).
13. Torbet, E. *et al.* A measurement of the angular power spectrum of the microwave background made from the high Chilean Andes. *Astrophys. J.* **521,** 79–82 (1999).
14. Miller, A. D. *et al.* A measurement of the angular power spectrum of the CMB from l = 100 to 400. *Astrophys. J.* (submitted); also as preprint astro-ph/9906421 at ⟨http://xxx.lanl.gov⟩ (1999).
15. Mauskopf, P. *et al.* Measurement of a peak in the CMB power spectrum from the test flight of BOOMERanG. *Astrophys. J.* (submitted); also as preprint astro-ph/9911444 at ⟨http://xxx.lanl.gov⟩ (1999).
16. Melchiorri, A. *et al.* A measurement of Ω from the North American test flight of BOOMERanG. *Astrophys. J.* (submitted); also as preprint astro-ph/9911445 at ⟨http://xxx.lanl.gov⟩ (1999).
17. de Bernardis, P. *et al.* Mapping the CMB sky: the BOOMERanG experiment. *New Astron. Rev.* **43,** 289–296 (1999).
18. Mauskopf, P. *et al.* Composite infrared bolometers with Si_3N_4 micromesh absorbers. *Appl. Opt.* **36,** 765–771 (1997).
19. Bock, J. *et al.* Silicon nitride micromesh bolometer arrays for SPIRE. *Proc. SPIE* **3357,** 297–304 (1998).
20. Masi, S. *et al.* A self contained ^{3}He refrigerator suitable for long duration balloon experiments. *Cryogenics* **38,** 319–324 (1998).
21. Masi, S. *et al.* A long duration cryostat suitable for balloon borne photometry. *Cryogenics* **39,** 217–224 (1999).
22. Schlegel, D. J., Finkbeiner, D. P. & Davis, M. Maps of dust IR emission for use in estimation of reddening and CMBR foregrounds. *Astrophys. J.* **500,** 525–553 (1998).
23. Delabrouille, J., Gorski, K. M. & Hivon, E. Circular scans for CMB anisotropy observation and analysis. *Mon. Not. R. Astron. Soc.* **298,** 445–450 (1998).
24. Cheung, L. H. *et al.* 1.0 millimeter maps and radial density distributions of southern HII/molecular cloud complexes. *Astrophys. J.* **240,** 74–83 (1980).
25. Kogut, A. *et al.* Dipole anisotropy in the COBE DMR first-year sky maps. *Astrophys. J.* **419,** 1–6 (1993).
26. Tegmark, M. CMB mapping experiments: a designer's guide. *Phys. Rev. D* **56,** 4514–4529 (1997).
27. Bond, J. R., Crittenden, R., Jaffe, A. H. & Knox, L. E. Computing challenges of the cosmic microwave background. *Comput. Sci. Eng.* **21,** 1–21 (1999).
28. Borrill, J. in *Proc. 3K Cosmology EC-TMR Conf.* (eds Langlois, D., Ansari, R. & Vittorio, N.) 277 (American Institute of Physics Conf. Proc. Vol. 476, Woodbury, New York, 1999).
29. Prunet, S. *et al.* in *Proc. Conf. Energy Density in the Universe* (eds Langlois, D., Ansari, R. & Bartlett, J.) (Editiones Frontieres, Paris, 2000).
30. Gorski, K. M., Hivon, E. & Wandelt, B. D. in *Proc. MPA/ESO Conf.* (eds Banday, A. J., Sheth, R. K. & Da Costa, L.) (European Southern Observatory, Garching); see also ⟨http://www.tac.dk/~healpix/⟩.
31. Kogut, A. in *Microwave Foregrounds* (eds de Oliveira Costa, A. & Tegmark, M.) 91–99 (Astron. Soc. Pacif. Conf. Series. Vol 181, San Francisco, 1999).
32. Toffolatti, L. *et al.* Extragalactic source counts and contributions to the anisotropies of the CMB. *Mon. Not. R. Astron. Soc.* **297,** 117–127 (1998).
33. Wright, A. E. *et al.* The Parkes-MIT-NRAO (PMN) surveys II. Source catalog for the southern survey. *Astrophys. J. Supp. Ser.* **91,** 111–308 (1994); see also ⟨http://astron.berkeley.edu/wombat/foregrounds/radio.html⟩.
34. Borrill, J. in *Proc. 5th European SGI/Cray MPP Workshop* (CINECA, Bologna, 1999); Preprint astro-ph/9911389 at ⟨xxx.lanl.gov⟩ (1999); see also ⟨http://cfpa.berkeley.edu/~borrill/cmb/madcap.html⟩.
35. Durrer, R., Kunz, M. & Melchiorri, A. *Phys. Rev. D* **59,** 1–26 (1999).
36. Seljak, U. & Zaldarriaga, M. A line of sight approach to cosmic microwave background anisotropies. *Astrophys. J.* **437,** 469–477 (1996).
37. Lewis, A., Challinor, A. & Lasenby, A. Efficient computation of CMB anisotropies in closed FRW models. Preprint astro-ph/9911177 at ⟨http://xxx.lanl.gov⟩ (1999).
38. Efstathiou, G. & Bond, R. Cosmic confusion: degeneracies among cosmological parameters derived from measurements of microwave background anisotropies. *Mon Not. R. Astron. Soc.* **304,** 75–97 (1998).
39. Wright, E. *et al.* Comments on the statistical analysis of excess variance in the COBE-DMR maps. *Astrophys. J.* **420,** 1–8 (1994).
40. Perlmutter, S. *et al.* Measurements of and Λ from 42 high-redshift supernovae. *Astrophys. J.* **517,** 565–586 (1999).
41. Schmidt, B. P. *et al.* The high-Z supernova search: measuring cosmic deceleration and global curvature of the Universe using type Ia supernovae. *Astrophys. J.* **507,** 46–63 (1998).

Acknowledgements

The Boomerang experiment was supported by Programma Nazionale di Ricerche in Antartide, Universita' di Roma "La Sapienza", and Agenzia Spaziale Italiana in Italy, by the NSF and NASA in the USA, and by PPARC in the UK. We thank the staff of the National Scientific Ballooning Facility, and the United States Antarctic Program personnel in McMurdo for their preflight support and an effective LDB flight. DOE/NERSC provided the supercomputing facilities.

Correspondence and requests for materials should be addressed to P. d. B. (e-mail: debernardis@roma1.infn.it). Details of the experiment and numerical data sets are available at the web sites ⟨http://oberon.roma1.infn.it/boomerang⟩ and ⟨http://www.physics.ucsb.edu/~boomerang⟩.

© 2000 Macmillan Magazines Ltd